

Article

Lattice Rotation Dependence on Microstructural Characteristics in a Low Carbon Steel

Satish K. Shekhawat¹, Rajesh K. Khatirkar^{2,*} and Murat Demiral^{3,*} 

¹ Powergrid Corporation of India Limited, Technology Development Department, PARTeC, Panchgaon, Manesar, Gurgaon 122413, Haryana, India; satishshekhawat@powergrid.in

² Department of Metallurgical and Materials Engineering, Visvesvaraya National Institute of Technology (VNIT), South Ambazari Road, Nagpur 440010, Maharashtra, India

³ College of Engineering and Technology, American University of the Middle East, Egaila 54200, Kuwait

* Correspondence: rajeshk@mme.vnit.ac.in (R.K.K.); murat.demiral@aum.edu.kw (M.D.)

Abstract: The lattice rotation behavior of low-carbon (LC) steel subjected to tensile deformation was studied by electron backscatter diffraction (EBSD). The EBSD scans of the same region were taken before and after tensile deformation. The rotation of the grains was found to depend on a number of factors like the initial orientation, the size of the grains, the number of neighboring grains and the region of the grain. The region near the grain boundaries was found to have significant deviation from that of the interior of the grain. The lattice rotations were also simulated using DAMASK software. The simulations gave information about the state of stress for each grain and the strain gradients developed during the deformation. The orientation dependence of misorientation and geometrically necessary dislocations (GNDs) was also studied. It was found that the misorientations changed more gradually in α -fiber grains than in γ -fiber grains.

Keywords: EBSD; grain rotation; DAMASK; GNDs



Citation: Shekhawat, S.K.; Khatirkar, R.K.; Demiral, M. Lattice Rotation Dependence on Microstructural Characteristics in a Low Carbon Steel. *Crystals* **2024**, *14*, 186. <https://doi.org/10.3390/cryst14020186>

Academic Editor: Kai Guan

Received: 24 December 2023

Revised: 29 January 2024

Accepted: 12 February 2024

Published: 13 February 2024



Copyright: © 2024 by the authors. Licensee MDPI, Basel, Switzerland. This article is an open access article distributed under the terms and conditions of the Creative Commons Attribution (CC BY) license (<https://creativecommons.org/licenses/by/4.0/>).

1. Introduction

Low-carbon steel is the perfect material for structural elements and welded constructions in a variety of industries, including construction and automobile manufacturing, because of its exceptional weldability, ductility and toughness. Its adaptability to applications needing a blend of strength and flexibility is highlighted by its resistance to deformation and capacity to absorb impact energy. Additionally, because of its lower cost in comparison to alloy and high-carbon steels, it is the material of choice for applications where high strength is not the only need, which helps to streamline manufacturing processes.

The mechanical properties of alloys, notably low-carbon steel, are intricately tied to several factors, with the initial grain size and texture and the size and distribution of second-phase particles playing pivotal roles. The evolution of the macroscopic texture in low-carbon steel is particularly influential, significantly impacting the engineering properties, a phenomenon directly linked to the crystal plasticity behavior of individual grains [1]. The development of deformation texture hinges on the activities of slip within specific slip systems. This induces a gradual rotation of grains from their initial orientation, allowing them to remain cohesive with neighboring grains and delaying fracture. The consequence of such slip activities in different regions of grains, coupled with the associated lattice rotation, leads to a substantial alteration in the shape of grains. This intricate interplay of factors underscores the complex nature of how mechanical properties are determined in low-carbon steel, highlighting the importance of understanding crystal plasticity and texture evolution for effective material design and engineering applications.

A few studies published in the literature examined the lattice rotation behavior of alloys including low-carbon steels. Zaeferer et al. [2] studied the low-alloyed TRIP steel's microstructure, transformation processes and the relationship between its microstructure

and mechanical qualities. The formation of the microstructure occurred when γ -grains expanded during inter-critical annealing and then shrank during the subsequent cooling process, all without the nucleation of new α -grains. Using a combination of optical microscopy (OM), scanning electron microscopy (SEM), electron backscattered diffraction (EBSD) and X-ray diffraction (XRD), Dutta et al. [3] examined the deformation microstructure beneath the area of ultrasonic treatment in the deformed samples. A considerable decrease in both the dislocation density and the fraction of low-angle grain boundaries together with preferred grain rotation was noticed. Recovery was correlated with a notable decrease in sub-grain development during deformation due to the ultrasound's softening impact. Nesterova [4] investigated the inter-relation between the microstructure and texture evolutions and their joint influence on the mechanical behavior. It was demonstrated that grains with well-developed pre-strain dislocation barriers and involvement with specific orientation groups exhibited a high localization of plastic flow inside microbands that followed an orthogonal strain-path mutation. Dhinwal et al. [5] studied the processing conditions' effects on texture and microstructure evolution during the multi-pass asymmetric rolling of extra-low-carbon steel. The applied thickness reduction during each pass, the sheet's overall thickness reduction and the degree of imposed asymmetry all had an impact on the development of both texture and microstructure. Gupta et al. [6] studied the relationship between strain path and microstructure with texture development in BCC Ti-15V-3Cr-3Sn-3Al alloy. It was observed that the texture growth was more strongly reliant on the strain path than the original microstructure during cold rolling. Mahadule et al. [7] analyzed the texture development during cold rolling in a Ti-15V-3Cr-3Sn-3Al alloy via experiments and numerical modeling based on crystal plasticity. It was observed that γ -(normal direction, ND//<111>) and α -(rolling direction, RD//<110>) fibers strengthened with cold rolling. Moura [8] studied the effect of crystallographic texture and the strain hardening behavior of UNS S32304 lean duplex stainless steel under a hot tensile test. Because of the austenite to ferrite phase transformation, the strain rate had an impact on the strain hardening behavior of duplex stainless steel. With an increase in strain rate, the transition strain between deformation phases grew. Nagarajan et al. [9] used in situ EBSD examination and crystal plasticity modeling to try and understand the impact of the coordinated deformation of polycrystalline Al-Mg alloy on its lattice rotation behavior during tensile deformation. It was observed that more rotations of grains were possible than the number of slip systems that were triggered during deformation. A potential shortest path rotated directly to the nearby stable end orientation when the misorientations shared by the immediate neighbors were more than 30°. Liu et al. [10] investigated the deformation mechanism in terms of slip behavior, the evolution of a grain boundary and the development of geometrically necessary dislocations (GNDs) for ferrite in a low-carbon Al-killed steel. While the microstructural unit size limited the dislocation's mobility, small grains were more likely to collect GNDs. Grain orientation had less of an impact on all grains when their Schmid Factor (SF) was high. An in situ EBSD analysis of nickel-based superalloy deformation behavior during uniaxial tensile tests was conducted by Zhang et al. [11]. As strain increased, the average misorientation angle rose and subsequently fell, and this was related to the number of dislocations. A number of coordinated strengthening mechanisms worked together during the deformation process to boost the alloy's strength. Chen and Wang [12] conducted a comparable work in which they examined 409 L ferritic stainless steel in situ using EBSD during tensile testing. The tensile axis of the rolling direction specimens rotated in the direction of <101> during tensile deformation, which was the stable end orientation of body-centered cubic (BCC) metals. However, because less advantageous slip systems were in place in transverse-direction specimens, the rotation of the tensile axis towards <101> was constrained. In both specimens, the most advantageous slip system was {110}<111>. Mehmet Sahin Atas et al. [13–15] studied model Ni-15Al, Ni-Al-Y and Ni-Al-Nb superalloys and showed that aging time significantly influenced the size, shape and type of precipitates in these systems. They also studied these systems ex situ.

Our main goal in this work is to use quasi in situ electron backscatter diffraction (EBSD) methods to examine the lattice rotation behavior of low-carbon steel under tension. Our analysis encompasses an examination of active slip systems, lattice rotation rates and rotation paths, with a particular focus on understanding the influence of misorientation and grain boundary segments shared with immediate neighbors. Additionally, we delve into the nuances of the kinematics associated with local lattice reorientation induced by second-phase particles, slip plane kinking and the inherent deformation heterogeneity across neighboring grains. In tandem with experimental findings, the study employs DAMASK software for the simulation of lattice rotations. This computational approach not only validates experimental observations but also provides a deeper understanding of the stress states within grains and the evolving strain gradient during deformation. The integration of experimental and simulated results offers a holistic perspective on the mechanical intricacies at the microstructural level.

2. Materials and Methods

2.1. Material and Processing

The chemical composition of the low carbon used in the present investigation was determined by optical emission spectroscopy (OES) and is given in Table 1. The initial sheet was 0.5 mm thick.

Table 1. Chemical composition (in weight% alloying elements) of the low-carbon steel.

	C	Mn	Al	Si	P	Cr	Fe
LC steel	0.008	0.33	0.22	0.50	0.05	0.011	Balance

In order to investigate the effect of deformation on grain rotation, tensile tests were carried out. The tensile specimen was prepared along the rolling direction (RD) as per ASTM E8 [16]. The gauge section of the tensile specimen was metallographically polished followed by electropolishing, and finally, sub-micron colloidal silica [17–19] was used to carry out the EBSD investigations before and after deformation. A square region was considered, and to identify same region before and after deformation, one microindentation was placed at each corner. Tensile tests were carried out on an INSTRON™ 3345 machine at a cross head speed of 1 mm/min. The experiments were repeated at strains of 2%, 3%, 5% and 7%, and the same area underwent EBSD microstructural analysis. To monitor the rotation and deformation behavior of the same grain (or region), interrupted tests were required.

2.2. Microstructure Characterization

EBSD was used to characterize the microstructure. The initial sample (before deformation) was electropolished with an electrolyte consisting of a mixture of ethanol and perchloric acid at a ratio of 80:20 (by volume) with Struer's Letropol-5™ electro-polisher for 30 s at 18 V DC and 0 °C. EBSD measurements were conducted on an FEI Quanta 200HV scanning electron microscope (SEM) equipped with an EDAX, USA, EBSD system. The step size used was 1 μm to cover a large area. To prevent any negative impact on the quality of the data, the camera settings were maintained throughout the scanning process for every sample. EBSD data were post processed with TSL 7.2 software [20], and all the data points with questionable accuracy, i.e., confidence index CI < 0.1 [21], were neglected during the analysis. Kernel average misorientation [22], the density of geometrically necessary dislocation [23] and grain orientations were tracked during deformation.

2.3. Crystal Plasticity (CP) Tensile Simulations

CP tensile simulations were carried out using the open source code Düsseldorf Advanced Material Simulation Kit (DAMASK) [24] with the integrated spectral solver. The orientation input files were generated from the experimental EBSD data of the initial unde-

formed sample. In the next section, the constitutive equations used in the simulations are summarized.

The deformation gradient splits into a plastic and elastic component through multiplication as follows:

$$F = F^e F^p, \quad (1)$$

where F^e denotes the rotation and elastic distortion of the crystal lattice and F^p represents the inelastic shear deformation on the slip planes.

The following generalized Hook's Law is used to calculate the material's stress response:

$$S = C : E, \quad (2)$$

with S being the Second Piolo–Kirchoff stress, C the forth-order anstropic elastic tensor and E the Green–Lagrange strain.

The shear contributions of the slip systems α make up the plastic velocity gradient as follows:

$$L^p = \sum_{\alpha} \dot{\gamma}^{\alpha} m^{\alpha} \otimes n^{\alpha}, \quad (3)$$

where $\dot{\gamma}^{\alpha}$ is the slip rate of the slip system, m^{α} the slip direction and n^{α} the normal to the slip plane which forms the Schmidt tensor.

The shear rates of the slip systems α are calculated in relation to the selected material model as follows:

$$\dot{\gamma}^{\alpha} = \dot{\gamma}_0^{\alpha} \left| \frac{\tau^{\alpha}}{g^{\alpha}} \right|^n \text{sgn}(\tau^{\alpha}), \quad (4)$$

with $\dot{\gamma}_0^{\alpha}$ being the reference slip rate, τ^{α} determining the resolved shear stress, n denoting the rate sensitivity and g^{α} being the slip resistance of the respective slip system.

After that, the slip resistance itself asymptotically changes from an initial value of g_0^{α} to a saturation value of g_{sat}^{α} using the following equation:

$$\dot{g}^{\alpha} = h_0 \left| \dot{\gamma}^{\beta} \right| \left| 1 - \frac{g^{\beta}}{g_{sat}^{\beta}} \right|^{\alpha} \text{sgn} \left(1 - \frac{g^{\beta}}{g_{sat}^{\beta}} \right) h^{\alpha\beta}. \quad (5)$$

Here, h_0 and α represent the self-hardening coefficient and the hardening exponent, respectively, and $h^{\alpha\beta}$ is components of the slip interaction matrix with a value of 1.0 and 1.4 for coplanar and non-coplanar slip systems, respectively.

The constants used in CP tensile simulations using DAMASK are given in Table 2, taken from Refs. [25,26]. The simulations were carried out with a step size of 0.0001 considering two slip systems ($\{110\}\langle 111 \rangle + \{112\}\langle 111 \rangle$). The tensile boundary conditions were defined using the strain matrix $[1 \ 0 \ 0, \ 0 \ -0.5 \ 0, \ 0 \ 0 \ -0.5]$.

Table 2. Material parameters of low-carbon steel used in CP simulations.

Parameter	Value
C_{11}	233.3 GPa
C_{12}	135.5 GPa
C_{44}	118.0 GPa
$\dot{\gamma}_0^{\alpha}$	0.001 1/s
h_0	1000 MPa
n	20
α	2

Table 2. Cont.

Parameter	Value
δ_0^α	95 MPa {110}
	97 MPa {112}
δ_{sat}^α	222.0 MPa {110}
	412.7 MPa {112}

3. Results and Discussion

Figure 1 shows the true stress–true strain curve and $\varphi_2 = 45^\circ$ constant section of the orientation distribution function (ODF) [27] of the LC steel used in the present investigation. The stress–strain curve shows that the material work hardened with an increase in deformation. The ductility was around 20%. The ODF showed a pronounced γ -fiber (ND//<111>) texture with significant Goss ({110}<100>). An exact cube ({100}<100>) was not present, but near-cube components were present. The spread around the cube was ~ 10 – 15° [27].

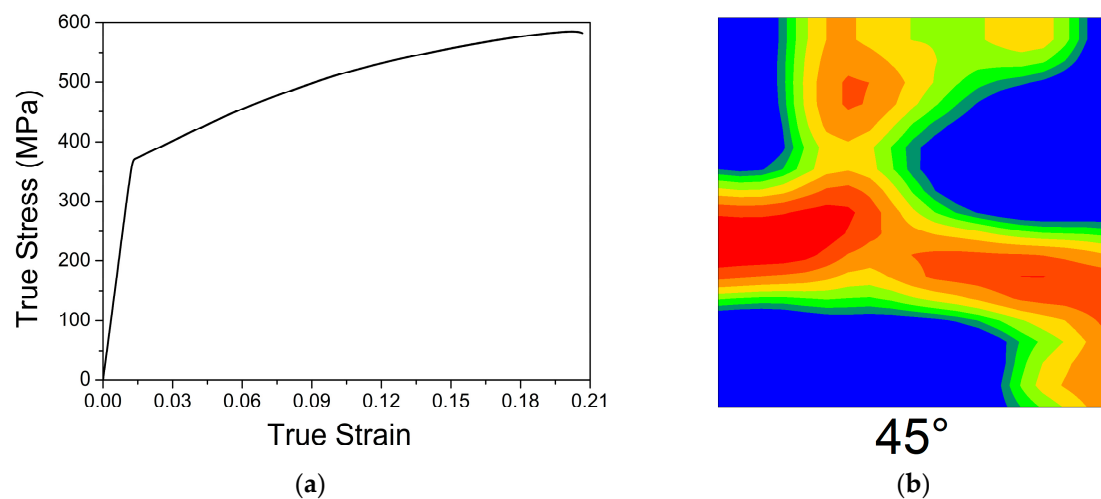


Figure 1. (a) True stress–true strain curve for the LC steel used in the present investigation. The tests were interrupted at a strain of 0.03, 0.05 and 0.05 for microstructural characterization. (b) $\varphi_2 = 45^\circ$ constant section of the orientation distribution function (ODF) for the initial material.

Figure 2 shows the distribution of KAM with the increase in tensile strain. As expected, KAM increased with an increase in deformation. The increase in green color signifies an increase in the magnitude of KAM. KAM is expected to scale with GNDs, i.e., excess dislocations [28]. The excess dislocations are expected to create large misorientations in the vicinity. Statistically stored dislocations (SSDs) are redundant and do not give rise to an increase in misorientations. It can be clearly seen that the near-boundary zone had higher GNDs than the interior of the grains. These were visible at small deformations, usually less than 10%. After 10% deformation, the dislocation density became too large to be clearly resolved and, hence, the increase in misorientation saturated. Figure 3 shows the overall GND distribution for the entire scanned area. The GND number fraction increased to a higher value with the increase in deformation, i.e., the strain. Both distributions of the KAM map and GND indicated the increase in dislocations with an increase in the deformation [29].

The developments in misorientations are also expected to be orientation-sensitive and depend on a number of factors including the grain size, the number of nearest neighbors and their misorientations, etc. Therefore, it is very difficult to quantify this phenomenon. However, it has also been reported that the near-boundary gradient zone also plays an important role. The DAMASK simulation results (Figure 4) indicated an increase in the

stress level with an increase in strain. There was also a significant change in the overall orientation distribution. However, it was clear that some grains rotated more than others after the deformation. The IPF map, i.e., the bottom row of Figure 4, shows that some grains completely reoriented after deformation, even if the deformation was very small. In order to gain more clarity on this, 15 grains were studied in the present work. These grains were selected randomly to understand this phenomenon.

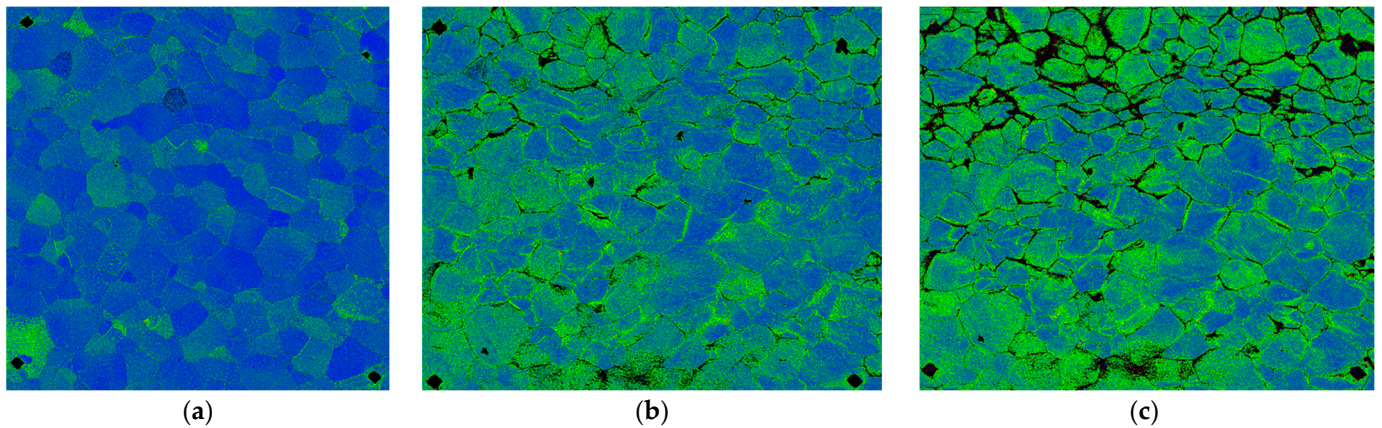


Figure 2. The distribution of Kernel average misorientation (KAM) of the undeformed (a), 3% deformed (b) and 7% deformed (c) sheet. 0° – 5° is the color scale.

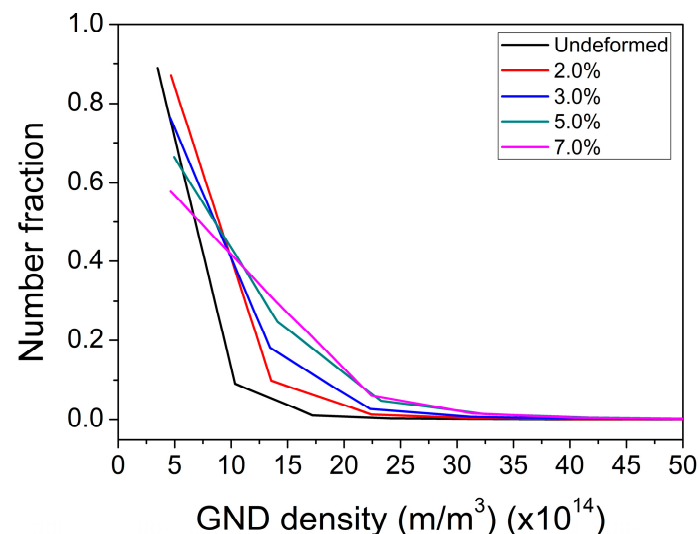


Figure 3. Geometrically necessary dislocation density (GND) distribution for undeformed and deformed samples.

As seen in Figure 5, 15 grains were chosen at random to observe grain rotation during deformation. The grain identification is marked for the undeformed IPF map as numbers from 1 to 15 (see Figure 5a). It can be seen from Figure 5b–d that there was a significant change in the color of the grains. This change implies that during deformation, the grains rotated and generated orientation gradients. After around 7% strain, the larger grains such as the ones numbered 1, 12 and 13 led to the development of significant spread and also their gradients. This gradient was more apparent near the grain boundaries. It has been reported [30] that this orientation gradient near grain boundaries, often termed as the near-boundary gradient zone (NBGZ), is responsible for the changes in texture during deformation. The cube grains (4, 7, 8 and 9) were found to be relatively more stable than the others, i.e., other orientations. Figure 6 shows the IPF for the undeformed and deformed conditions for these 15 grains.

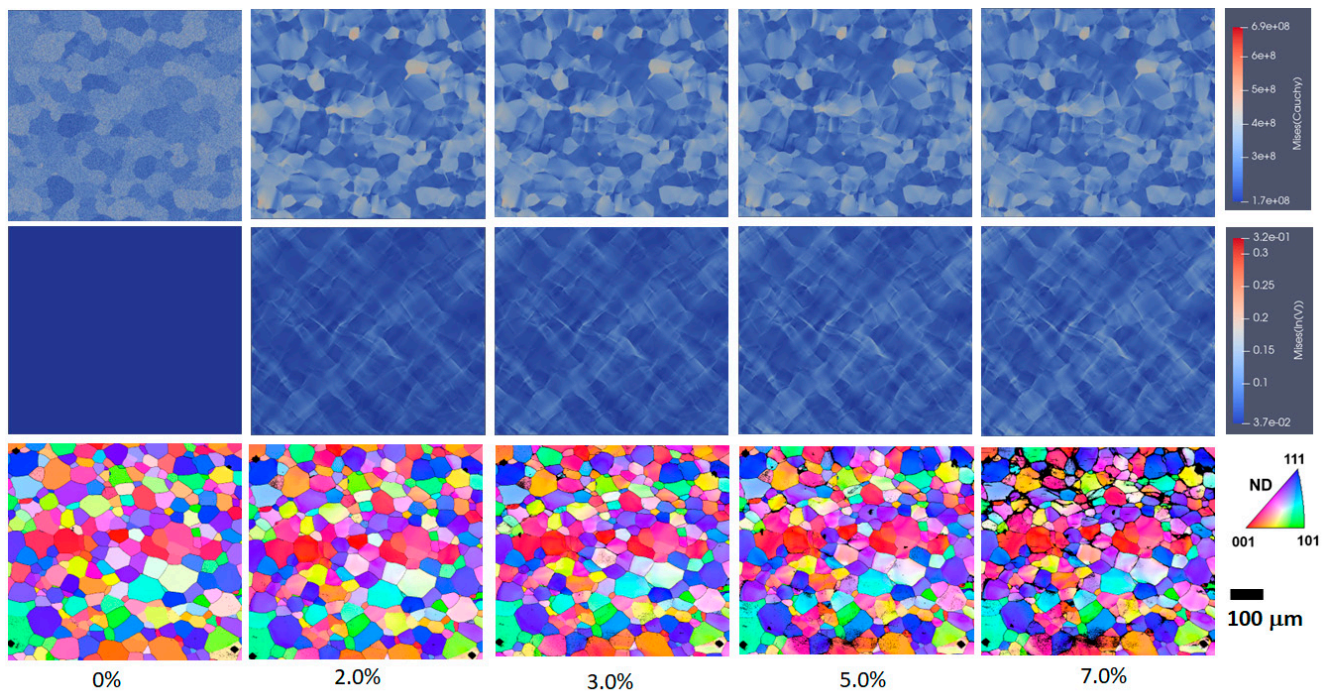


Figure 4. The von-Mises stress (top row), von-Mises strain (middle row) and inverse pole figure (IPF) map (bottom row) after DAMASK simulations.

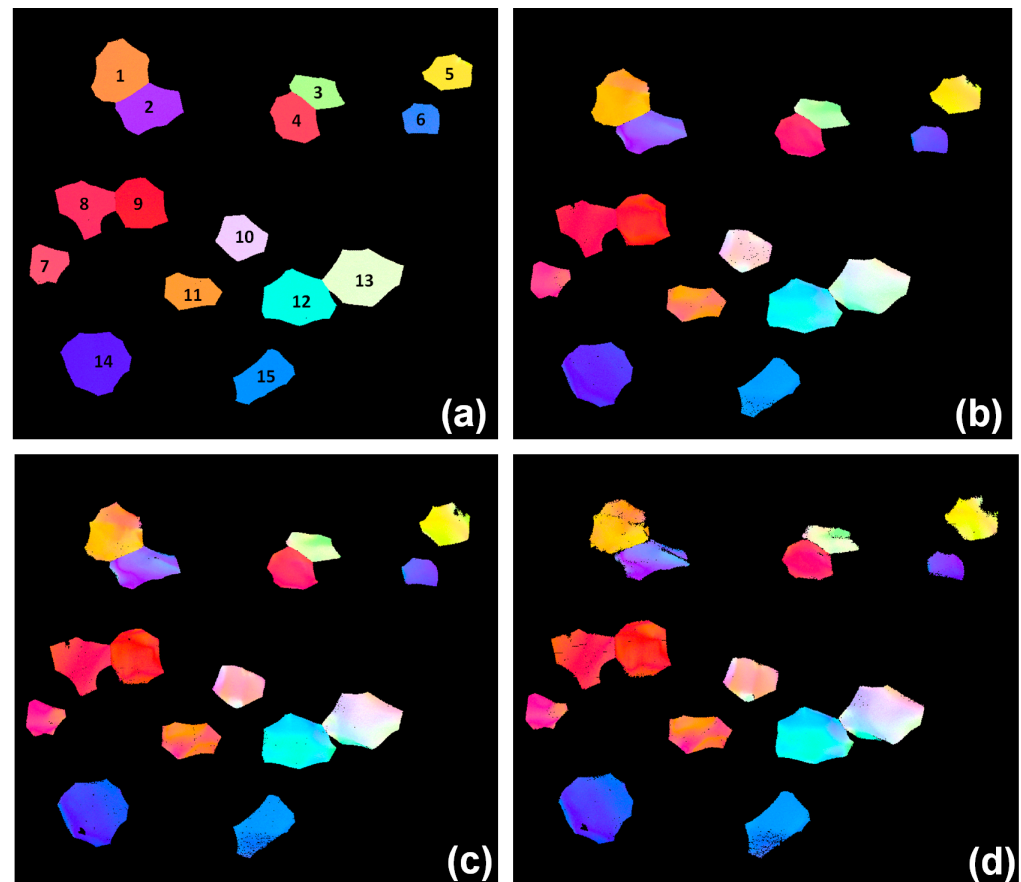


Figure 5. ND IPF map of the 15 grains tracked during deformation. (a) Undeformed, (b) after 3% strain, (c) after 5% strain and (d) after 7% strain.

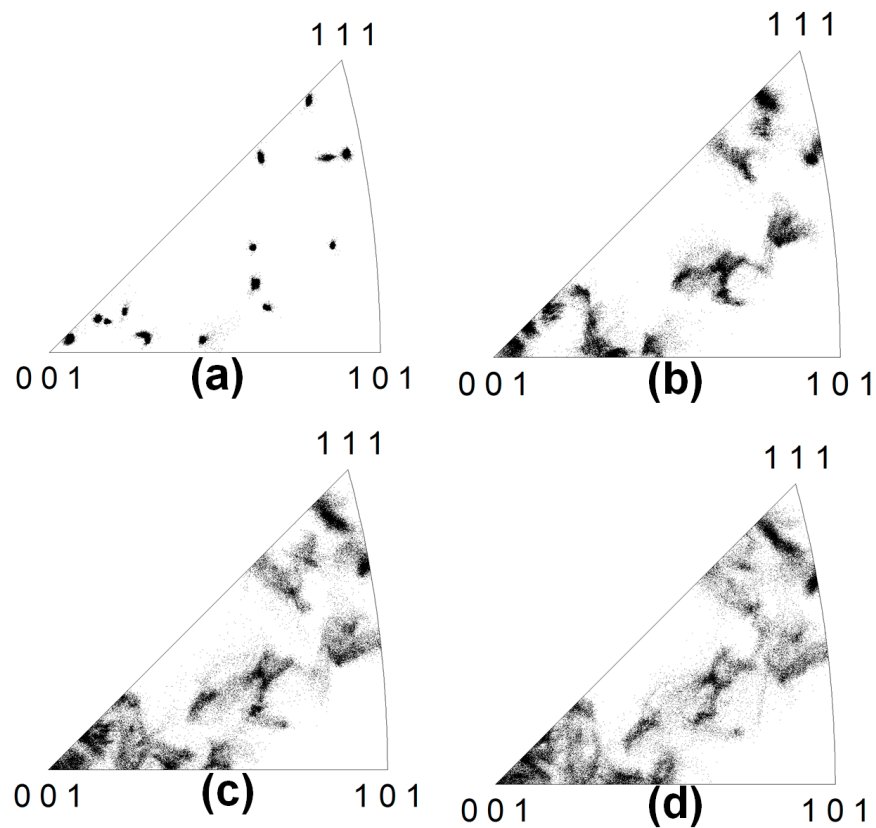


Figure 6. ND IPF of the 15 grains showing rotation and orientation spread during deformation. (a) Undeformed, (b) after 3% strain, (c) after 5% strain and (d) after 7% strain.

γ -fiber (ND// $\langle 111 \rangle$) grains also developed gradients, but these grains did not move away significantly from the ND// $\langle 111 \rangle$ orientation. Grains which had orientations other than cube and γ -fiber showed significant rotations. This is very clearly visible in the IPF of Figure 6. Even after 7% strain, the IPF changed to a very large extent, and, hence, after 10% deformation, BCC materials showed a change in crystallographic texture independent of the mode of deformation (tensile, compression or cold rolling). Table 3 gives numerical values of the orientation, grain size, GOS and number of neighbors for these 15 grains. The grain size and initial orientation seemed to be the most important parameters governing the grain rotation and hence texture change during the deformation.

It is always believed that the rotation of grains occurs from unstable to stable end orientations during deformation. Inagaki [31–34] has shown that in polycrystalline iron, grain boundary constraints play an important role in the formation of cold deformation texture. In poly-crystals, crystal rotation occurs during rolling along different paths from that observed in single crystals [35]. It was found that crystal rotations occur along two paths (Path A: $\{001\}\langle 100 \rangle$ to $\{001\}\langle 110 \rangle$ to $\{112\}\langle 110 \rangle$ to $\{223\}\langle 110 \rangle$ and Path B: $\{110\}\langle 001 \rangle$ to $\{554\}\langle 225 \rangle$ to $\{111\}\langle 112 \rangle$ to $\{111\}\langle 110 \rangle$ to $\{223\}\langle 110 \rangle$). The stable end orientation of cold rolling textures in poly-crystals was therefore identified as $\{223\}\langle 110 \rangle$. It was also suggested that $\{111\}\langle 112 \rangle$ orientations are unstable and rotate towards $\{111\}\langle 110 \rangle$ [31]. A strong γ -fiber (ND// $\langle 111 \rangle$) texture is developed if the initial orientation (before cold deformation) is $\{111\}\langle 112 \rangle$. If two $\{111\}\langle uvw \rangle$ -type grains are neighbors, their grain boundary regions rotate readily into common stable end orientation. It has been reported (using rate-dependent full constraint and relaxed constraint theory) that the principal component inherited from the recrystallized hot band, i.e., $\{100\}\langle 110 \rangle$, is a fairly stable end orientation and, hence, its intensity increases with cold rolling [36]. There is no concrete evidence of the exact mechanism of rotation of grains since it is a very complex phenomenon. However, it is clear that initial orientations represent one of the most important parameters

during deformation. To this end, if anyone wishes to customize the final crystallographic texture of a deformed or annealed material, the materials' initial crystallographic textures need to be customized.

Table 3. Orientation, grain size, number of neighbors and grain orientation spread (GOS) for the tracked grains.

Grain_ID	Phi1 (°)	Phi (°)	Phi2 (°)	Grain Size (µm)	# Neighbors	Grain Orientation Spread (GOS, °)			
						Undeformed	3% Strain	5% Strain	7% Strain
1	79.1	13.8	280.3	164.6	8	0.4	1.9	3.1	3.5
2	208.9	39.6	137.3	151.8	7	0.4	2.5	4.2	4.7
3	127.3	31	258.3	112.8	6	0.3	1.4	2.3	2.9
4	103.7	9.4	242	134.7	8	0.3	1.1	1.6	1.9
5	343.9	21.9	4.7	115.6	7	0.4	1.6	2.1	2.7
6	220	46.1	125	99.4	6	0.5	1.5	2	2.5
7	167.9	12.2	208.7	108.7	7	0.3	1.5	2.5	2.9
8	326.6	8.4	55.5	149.3	7	0.3	0.9	1.6	1.9
9	117.8	3.5	236.4	145.6	8	0.5	2.2	3.7	4.2
10	112.8	32	207.2	129.8	6	0.2	1.9	2.9	3.3
11	179.6	14.1	187	124.9	7	0.3	2.3	3.9	4.6
12	16.9	41.5	339.3	174.2	8	0.2	1.7	2.7	3.4
13	149.9	30.4	198.4	180.8	9	0.4	2	2.9	3.6
14	14.4	48.7	315.8	181	9	0.3	1.8	2.9	3.5
15	219.8	51.7	148.1	139.8	7	0.3	1.2	1.9	2.2

4. Conclusions

The following conclusions can be drawn from the present work:

- The rotation of grains towards stable end orientation depends largely on the initial orientation of the grains. Rotations are larger if the initial orientations deviate significantly from the stable end orientation.
- Large grains (in size) tend to develop large in-grain misorientations and lattice rotations along with NBGZ. They have a higher tendency to fragment than reorient.
- The mode of deformation and number of neighbors can be significant for the reorientation of grains. However, in the present investigation, the initial orientation of the grain was found to be more significant.

Author Contributions: S.K.S.—conceptualization, data curation, methodology, formal analysis, writing—original draft. R.K.K.—conceptualization, data curation, methodology, formal analysis, writing—review and editing, supervision. M.D.—conceptualization, data curation, methodology, formal analysis, writing—review and editing, supervision. All authors have read and agreed to the published version of the manuscript.

Funding: The APC was funded by the American University of the Middle East, Kuwait.

Data Availability Statement: The raw/processed data required to reproduce these findings cannot be shared at this time as the data also form a part of an ongoing study.

Acknowledgments: The authors would like to acknowledge the use of National Facility for Texture and the OIM—A DST-IRPHA project for EBSD measurements.

Conflicts of Interest: The authors declare no conflicts of interest.

References

1. Skrotzki, W.; Pukenas, A.; Odor, E.; Joni, B.; Ungar, T.; Völker, B.; Hohenwarter, A.; Pippan, R.; George, E.P. Microstructure, Texture, and Strength Development during High-Pressure Torsion of CrMnFeCoNi High-Entropy Alloy. *Crystals* **2020**, *10*, 336. [[CrossRef](#)]
2. Zaefferer, S.; Ohlert, J.; Bleck, W. A study of microstructure, transformation mechanisms and correlation between microstructure and mechanical properties of a low alloyed TRIP steel. *Acta Mater.* **2004**, *52*, 2765–2778. [[CrossRef](#)]

3. Dutta, R.K.; Petrov, R.H.; Delhez, R.; Hermans, M.J.M.; Richardson, I.M.; Böttger, A.J. The effect of tensile deformation by in situ ultrasonic treatment on the microstructure of low-carbon steel. *Acta Mater.* **2013**, *61*, 1592–1602. [[CrossRef](#)]
4. Nesterova, E.V.; Bacroix, B.; Teodosiu, C. Microstructure and texture evolution under strain-path changes in low-carbon interstitial-free steel. *Met. Mater. Trans. A* **2001**, *32*, 2527–2538. [[CrossRef](#)]
5. Dhinwal, S.S.; Toth, L.S.; Hodgson, P.D.; Haldar, A. Effects of Processing Conditions on Texture and Microstructure Evolution in Extra-Low Carbon Steel during Multi-Pass Asymmetric Rolling. *Materials* **2018**, *11*, 1327. [[CrossRef](#)]
6. Gupta, A.; Khatirkar, R.K.; Kumar, A.; Thool, K.; Bibhanshu, N.; Suwas, S. Microstructure and texture development in Ti-15V-3Cr-3Sn-3Al alloy—Possible role of strain path. *Mater. Charact.* **2019**, *156*, 109884. [[CrossRef](#)]
7. Mahadule, D.; Demiral, M.; Mulki, H.; Khatirkar, R.K. Experiments and Crystal Plasticity Finite Element Simulations of Texture Development during Cold Rolling in a Ti-15V-3Cr-3Sn-3Al Alloy. *Crystals* **2023**, *13*, 137. [[CrossRef](#)]
8. de Moura, A.N.; Neto, C.A.R.; Castro, N.A.; Vieira, E.A.; Orlando, M.T.D.A. Microstructure, crystallographic texture and strain hardening behavior in hot tensile tests of UNS S32304 Lean Duplex stainless steel. *J. Mater. Res. Technol.* **2021**, *12*, 1065–1079. [[CrossRef](#)]
9. Nagarajan, S.; Jain, R.; Gurao, N.P. Microstructural characteristics governing the lattice rotation in Al-Mg alloy using in-situ EBSD. *Mater. Charact.* **2021**, *180*, 111405. [[CrossRef](#)]
10. Liu, M.; Liu, Y.; Li, H. Deformation mechanism of ferrite in a low carbon Al-killed steel: Slip behavior, grain boundary evolution and GND development. *Mater. Sci. Eng. A* **2022**, *842*, 143093. [[CrossRef](#)]
11. Zhang, C.; Ya, R.; Sun, M.; Ma, R.; Cui, J.; Li, Z.; Tian, W. In-situ EBSD study of deformation behavior of nickel-based superalloys during uniaxial tensile tests. *Mater. Today Commun.* **2023**, *35*, 105522. [[CrossRef](#)]
12. Chen, J.; Wang, J. In-situ EBSD study of 409 L ferritic stainless steel during tensile testing. *Mater. Res. Express* **2022**, *9*, 116508. [[CrossRef](#)]
13. Atas, M.S.; Yildirim, M. Temporal evolution, coarsening behavior and oxidation resistance of Ni-15Al superalloy. *J. Alloys Compd.* **2019**, *9*, 151784. [[CrossRef](#)]
14. Atas, M.S.; Yildirim, M. Structural properties and cyclic oxidation behavior of Ni-Al-Y superalloys. *Kokove Mater.* **2022**, *60*, 281–292.
15. Atas, M.S.; Yildirim, M. Morphological developments, coarsening and oxidation behavior of Ni-Al-Nb superalloys. *J. Mater. Eng. Perform.* **2020**, *29*, 4421–4434. [[CrossRef](#)]
16. E8-04; Standard Test Method for Tensile Testing of Metallic Materials. ASTM: West Conshohocken, PA, USA, 2004.
17. Shekhawat, S.K.; Basavaraj, V.P.; Hiwarkar, V.; Chakrabarty, R.; Nemade, J.; Guruprasad, P.J.; Suresh, K.G.; Doherty, R.D.; Samajdar, I. Direct Experimental Observations on Concurrent Microstructure and Magnetic Property Developments in Non-Grain Oriented Electrical Steel. *Metall. Mater. Trans. A* **2014**, *45*, 3695–3698. [[CrossRef](#)]
18. Khatirkar, R.; Basavaraj, V.; Shekhawat, S.K.; Haldar, A.; Samajdar, I. Orientation Dependent Recovery in Interstitial Free Steel. *ISIJ Intl.* **2012**, *52*, 84–893. [[CrossRef](#)]
19. Khatirkar, R.; Krishna, K.V.M.; Kestens, L.A.I.; Petrov, R.; Pant, P.; Samajdar, I. Strain localization in ultra low carbon steel: Exploring the role of dislocations. *ISIJ Int.* **2011**, *51*, 849–856. [[CrossRef](#)]
20. OIM. *Analysis Version 7.2. User Manual*; TexSEM Laboratories Inc.: Draper, UT, USA, 2013.
21. Nowell, M.M.; Wright, S.I. Orientation effects on indexing of electron backscattered diffraction patterns. *Ultramicroscopy* **1984**, *103*, 41–58. [[CrossRef](#)] [[PubMed](#)]
22. Wright, S.I.; Nowell, M.M.; Field, D.P. A review of strain analysis using electron backscatter diffraction. *Microsc. Microanal.* **2011**, *17*, 316–329. [[CrossRef](#)] [[PubMed](#)]
23. Kundu, A.; Field, D.P. Geometrically Necessary Dislocation Density Evolution in Interstitial Free Steel at Small Plastic Strains. *Met. Mater Trans A* **2018**, *49*, 3274–3282. [[CrossRef](#)]
24. Roters, F.; Eisenlohr, P.; Kords, C.; Tjahjanto, D.D.; Diehl, M.; Raabe, D. DAMASK: The Düsseldorf advanced material simulation kit for studying crystal plasticity using an FE based or a spectral numerical solver. *Procedia IUTAM* **2012**, *3*, 3–10. [[CrossRef](#)]
25. Tasan, C.C.; Diehl, M.; Yan, D.; Zambaldi, C.; Shanthraj, P.; Roters, F. Integrated experimental-simulation analysis of stress and strain partitioning in multiphase alloys. *Acta Mater.* **2014**, *81*, 386–400. [[CrossRef](#)]
26. Deeparekha, N.; Gupta, A.; Demiral, M.; Khatirkar, R.K. Cold rolling of an interstitial free (IF) steel—Experiments and simulations. *Mech. Mater.* **2020**, *148*, 103420. [[CrossRef](#)]
27. Verlinden, B.; Driver, J.; Samajdar, I.; Doherty, R.D. *Thermo-Mechanical Processing of Metallic Materials*; Pergamon Materials, Series; Cahn, R.W., Ed.; Elsevier: Amsterdam, The Netherlands, 2007.
28. Field, D.P.; Trivedi, P.B.; Wright, S.I.; Kumar, M. Analysis of local orientation gradients in deformed single crystals. *Ultramicroscopy* **2005**, *103*, 33–39. [[CrossRef](#)]
29. Humphreys, F.J.; Hatherly, M. *Recrystallization and Related Annealing Phenomena*; Elsevier: Oxford, UK, 2004.
30. Mishra, S.; Pant, P.; Narasimhan, K.; Rollett, A.; Samajdar, I. On the widths of orientation gradient zones adjacent to grain boundaries. *Scr. Mater.* **2009**, *61*, 273–276. [[CrossRef](#)]
31. Inagaki, H. Fundamental Aspect of Texture Formation in Low Carbon Steel. *ISIJ Int.* **1994**, *34*, 313–321. [[CrossRef](#)]
32. Inagaki, H.; Suda, T. The developments of rolling textures in low-carbon steels. *Texture* **1972**, *1*, 129–140. [[CrossRef](#)]
33. Inagaki, H. Formation of {111} recrystallization texture in polycrystalline iron. *Trans. Iron Steel Inst. Jpn.* **1984**, *24*, 266–274. [[CrossRef](#)]

34. Inagaki, H. Stable End Orientations in the Rolling Textures of the Polycrystalline Iron. *Int. J. Mater. Res.* **1987**, *78*, 431–439. [[CrossRef](#)]
35. Demiral, M.; Roy, A.; El Sayed, T.; Silberschmidt, V.V. Influence of strain gradients on lattice rotation in nano-indentation experiments: A numerical study. *Mater. Sci. Eng. A* **2014**, *608*, 73–81. [[CrossRef](#)]
36. Khatirkar, R.K. Strain Localizations in Low Carbon Steels. Ph.D. Thesis, IIT Bombay, Mumbai, India, 2012.

Disclaimer/Publisher's Note: The statements, opinions and data contained in all publications are solely those of the individual author(s) and contributor(s) and not of MDPI and/or the editor(s). MDPI and/or the editor(s) disclaim responsibility for any injury to people or property resulting from any ideas, methods, instructions or products referred to in the content.